

# Real-Time Impedance Analysis for the On-Road Monitoring of Automotive Fuel Cells

Tim Lochner,<sup>\*,[a, b]</sup> Markus Perchthaler,<sup>[a]</sup> Janko T. Binder,<sup>[a]</sup> Jarek P. Sabawa,<sup>[a]</sup> Tuan Anh Dao,<sup>[a]</sup> and Aliaksandr S. Bandarenka<sup>\*,[b, c]</sup>

The on-road monitoring of polymer electrolyte membrane fuel cells (PEMFCs) in automotive systems optimizes their efficiency and fuel consumption in addition to increasing their lifetime. In this work, electrochemical impedance spectroscopy (EIS) measurements and special EIS data analysis algorithms were used to quickly identify fuel cell operational modes and failures during cell operation. The approach developed enables the measurement and analysis time of only a few seconds and allows the

accurate extraction of information about the membrane and charge transfer resistance. The data analysis procedures show similar accuracy to that of the complex non-linear least square fitting algorithms. As a result, typical operational failures like air and hydrogen starvation were able to be easily distinguished, and different operational states (membrane humidification, air stoichiometry) of the PEMFCs could be identified.

## 1. Introduction

In 2022, the BMW Group will present the next-generation of hydrogen fuel cell (FC) electric drive systems in a small-series vehicle.<sup>[1]</sup> For automotive applications, the polymer electrolyte membrane fuel cell (PEMFC) is the most common FC type. PEMFCs make it possible to achieve environmentally-friendly operation with high driving ranges and short refueling times.<sup>[2,3]</sup> During PEMFC operation, a variety of failure modes can occur that impact the FC lifetime and efficiency. The operational strategy of the FC systems tends to optimize the PEMFC stack operating conditions. Thereby, this strategy relies on information about the origin of the failure to prevent FC degradation and to increase its efficiency. Automotive PEMFC systems typically consist of 300 to 400 stacked FCs. Commonly, cell voltage monitoring of single cells or cell arrays is implemented since it represents a simple monitoring technique.<sup>[4]</sup> However, multiple faults can cause the cell voltage to drop. Therefore, monitoring only the cell voltage is insufficient for identifying the origin of the problems.<sup>[4]</sup> Some operational effects that impact FC durability and efficiency include media starvation, catalyst poisoning and flooding as well as dehydration of the

electrode layers.<sup>[5]</sup> Electrochemical Impedance Spectroscopy (EIS) can be used as a non-destructive and “on-line” diagnostic tool that identifies these faults and analyzes the PEMFC operation.<sup>[6,7,8,9]</sup> Therefore, it can be used for state-of-health determination and for predictive control strategies in automotive FC applications.<sup>[10–14]</sup> The importance of this topic can be seen by the high patent registration effort of most companies that are developing fuel cell electric vehicles, such as Toyota, Hyundai, Nissan and Honda.<sup>[15–18]</sup> Implementation of EIS into the automotive systems requires a minimal number of sensors.<sup>[19–21]</sup> Impedance measurements in automotive applications need to fulfill certain criteria, as listed below.


1. Data acquisition time needs to be less than 1 s due to the fluctuating system conditions<sup>[22,23]</sup> and due to operational faults that lead to severe FC degradation within seconds.<sup>[24,25]</sup>
2. Mathematical analysis algorithms should be fast (e.g., analytical) and stable (e.g., independent of initial parameter sets).<sup>[26,27]</sup>
3. EIS measurement parameters should allow a simple physical interpretation with respect to the operational parameters (e.g., polymer humidification,<sup>[6]</sup> oxygen partial pressure<sup>[7])</sup> and FC failures (e.g., hydrogen starvation, flooding).<sup>[6,10–12]</sup>
4. Reasonable accuracy. The required accuracy depends on the sensitivity of the EIS parameters on the operational parameters and FC failures.<sup>[22]</sup>


Several impedance-based methodologies exist for characterizing the FCs. Total harmonic distortion analysis is a powerful tool used to detect various FC failure modes.<sup>[28,29]</sup> So far, only a few publications exist which deal with the physical interpretation using these harmonic responses for PEMFCs.<sup>[30]</sup> Distribution of relaxation times (DRT) is a data processing procedure to analyze EIS data. DRT calculations rely on high quality datasets; otherwise, the resulting DRT spectrum contains significant errors.<sup>[31]</sup> In electrically noisy automotive systems, the DRT analysis might therefore lead to misinterpretations and cause fatal instabilities. Other impedance monitoring techniques are based on the analysis at single frequencies.<sup>[11,12]</sup> Measuring the

[a] T. Lochner, Dr. M. Perchthaler, J. T. Binder, J. P. Sabawa, T. A. Dao  
BMW Group, 80809 München, Germany  
E-mail: tim.lochner@bmw.de

[b] T. Lochner, Prof. A. S. Bandarenka  
Physik-Department ECS, Technische Universität München, James-Frank-Str.  
1, 85748 Garching, Germany  
E-mail: bandarenka@ph.tum.de

[c] Prof. A. S. Bandarenka  
Catalysis Research Center, Technical University of Munich, Ernst-Otto-  
Fischer-Str. 1, 85748 Garching, Germany

 Supporting information for this article is available on the WWW under <https://doi.org/10.1002/celec.202000510>

 © 2020 The Authors. Published by Wiley-VCH Verlag GmbH & Co. KGaA. This is an open access article under the terms of the Creative Commons Attribution License, which permits use, distribution and reproduction in any medium, provided the original work is properly cited. Open access funding enabled and organized by Projekt DEAL.

impedance at only one or two frequencies is a fast technique, but interpretation can nevertheless be difficult when, e.g., neglecting effects of the double layer capacitance. In addition to EIS, other techniques like current pulse injection (CPI) have also been successfully implemented as fuel cell diagnostic tools. CPI extracts similar diagnostic criteria to EIS by reducing measurement costs compared to the traditional EIS measurement instrumentation.<sup>[32]</sup>

In laboratory experiments, EIS spectra of PEMFCs are typically acquired in a wide frequency range and afterwards analyzed using complex non-linear least square (CNLS) fitting to an equivalent electric circuit (EEC).<sup>[33–36]</sup> This results in measurement times in the range of minutes as well as slow and instable data processing.<sup>[26]</sup> Differential impedance analysis (DIA) is an alternative EIS data post processing approach.<sup>[37]</sup> Its modification for enabling the real-time analysis was previously implemented in the “on-line” monitoring of living tissues.<sup>[27]</sup> For the PEMFC, in order to determine typical EEC elements, e.g., the membrane resistance ( $R_{\text{mem}}$ ), the charge transfer resistance ( $R_{\text{ct}}$ ), and the double layer capacitance ( $C_{\text{DL}}$ ) (see Figure 1A), DIA should rely on a minimum of 3 measurement frequencies in the high frequency region (50 to 1000 Hz). This would allow a quick determination of the EEC parameters. The purpose of this study is to evaluate DIA as a real-time diagnostic tool for monitoring the normal and faulty operation of fuel cell electric vehicles. The goal of the measurement is to extract information on the membrane resistance, cathode resistance, and double layer capacitance of an automotive PEMFC in real time.

## Computational Methods

### Concept of Data Evaluation

The approach presented here relied on the impedance measurement of a fuel cell at several (at least three) frequencies  $f$  (or angular frequencies  $\omega$ ). The impedance at a certain frequency  $\omega$  was thereby commonly separated into resistance  $Z_{\text{Re}}$  and reactance  $Z_{\text{Im}}$ . DIA relies on the aforementioned parameters ( $\omega$ ,  $Z_{\text{Re}}$ ,  $Z_{\text{Im}}$ ) as

well as on their derivatives ( $\frac{\partial Z_{\text{Im}}}{\partial \omega}$ ,  $\frac{\partial Z_{\text{Re}}}{\partial \omega}$ ) to calculate  $R_{\text{mem}}$ ,  $R_{\text{ct}}$  and  $C_{\text{DL}}$  of a Randles EEC (see Figure 1A). Based on the derivatives of effective inductance  $\partial L_{\text{eff}}(\omega)$  and the resistance  $\partial Z_{\text{Re}}(\omega)$ , the time-constant  $T(\omega)$  is defined in Eq. 1.

$$T(\omega) = \frac{\partial L_{\text{eff}}(\omega)}{\partial Z_{\text{Re}}(\omega)} \quad (1)$$

This allows the calculation of the charge transfer resistance  $R_{\text{ct}}$  (Eq. 2):

$$R_{\text{ct}}(\omega) = -\frac{\partial Z_{\text{Re}}(\omega)}{\partial \omega} \cdot \frac{(1 + \omega^2 T^2)^2}{2\omega T^2} \quad (2)$$

Based on  $T$  and  $R_{\text{ct}}$  the membrane resistance of the fuel cell  $R_{\text{mem}}$  can be derived (Eq. 3):

$$R_{\text{mem}}(\omega) = Z_{\text{Re}}(\omega) - \frac{R_{\text{ct}}(\omega)}{1 + \omega^2 T^2} \quad (3)$$

Finally, the double layer capacitance of the fuel cell can be obtained as formulated in Eq. 4.

$$C_{\text{DL}}(\omega) = \frac{T(\omega)}{R_{\text{ct}}(\omega)} \quad (4)$$

Eq. 1 to Eq. 4 are derived in detail elsewhere.<sup>[37]</sup> In summary, DIA allows determination of Randles EEC parameters based on analytical equations.

To demonstrate the usefulness of the DIA equations, a Randles EEC with fixed resistances and three different values of the double layer capacitance was modeled. The model parameters were based on typical automotive size values, as will be described later (Figure 6). The modeled EEC and its parameters are indicated in Figure 1A. The corresponding Bode plots in Figure 1 B indicate that  $Z_{\text{Re}}$  at 300 Hz increases with a decreasing double layer capacitance. 300 Hz is a typical frequency used to measure FC system impedances due to inductive interferences at higher frequencies.<sup>[12]</sup> Using the value of  $Z_{\text{Re}}$  at 300 Hz to measure the membrane resistance can lead to overestimations of  $R_{\text{mem}}$ . Figure 1C plots the membrane resistance of the simulated EEC (Figure 1A) based on

### Impact of Double Layer Capacitance Variations on Impedance Response.

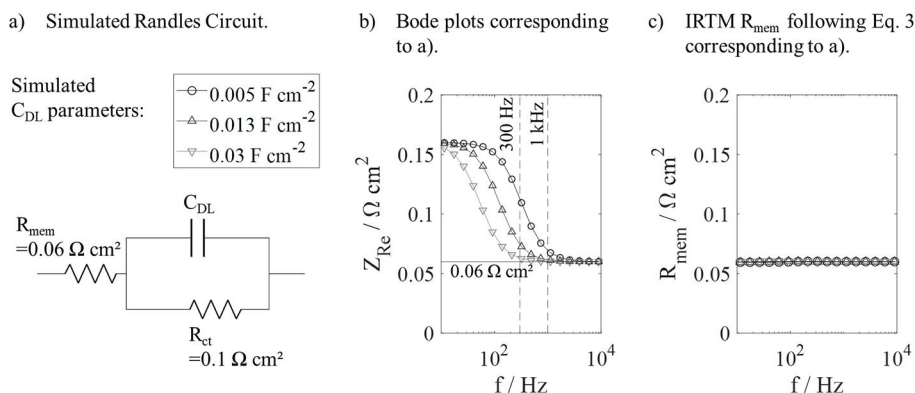


**Figure 1.** This figure illustrates how equation Eq. 3 can be used to identify the membrane resistance of a simple (simulated) Randles circuit. A) Randles circuit used to simulate impedance spectra. B) Bode plot  $Z_{\text{Re}}(f)$  of the simulated Randles circuit for three different double layer capacitances. The horizontal line represents the modeled  $R_{\text{mem}}$  value. The vertical lines indicate two frequencies (300 Hz, 1 kHz) that are typically used to measure the membrane resistance based on single frequencies. C)  $R_{\text{mem}}(f)$  calculation based on Eq. 3 for three different double layer capacitances ( $f = \frac{\pi}{2\pi}$ ).

calculations using Eq. 3. As can be seen, for all three double layer capacitances, the equation yields the simulated membrane resistance of  $0.06 \Omega \text{ cm}^2$ .  $R_{\text{mem}}$  in Figure 1C is insensitive to frequency. Therefore, the membrane resistance of a Randles EEC was able to be measured within a large frequency range using the DIA approach. In FC systems, this frequency range is limited to frequencies below 1 kHz due to inductive phenomena of the system, and to frequencies higher than 10–50 Hz due to interference with mass transport and oxygen oscillation mechanisms.<sup>[38,39]</sup>

### Impedance Real-Time Monitoring Approach

The Impedance Real-Time Monitoring (IRTM) methodology developed in this work used a linearization of equations Eq. 1 to Eq. 4 (for details see Figure S.3 supporting information). The IRTM procedure as implemented within this analysis is illustrated in Figure 2. A schematic Nyquist plot, obtained with EIS of a PEMFC is illustrated in Figure 2 (Step 1). Typically, Nyquist plots of PEMFCs look like a combination of one or two semicircles, where the left (high frequency) semicircle contains information on the membrane resistance,  $R_{\text{mem}}$  (left intercept with the x-axis), the charge transfer resistance,  $R_{\text{ct}}$ , and the double layer capacitance  $C_{\text{DL}}$ . The five points schematically indicated in blue in Figure 2 (Step 1) illustrate impedance data at different frequencies. The measurement frequencies need to be in the range of the left semicircle; this range is typically between 50 and 1000 Hz for PEMFCs. To calculate one set of EEC parameters ( $R_{\text{mem}}$ ,  $R_{\text{ct}}$ ,  $C_{\text{DL}}$ ), the data processing algorithm required at least 3 measurement frequencies.<sup>[37]</sup> Therefore, when recording the impedance at 5 frequencies, 3 different parameter

sets were extracted; this is indicated in Figure 2 (Step 2). The data processing algorithm calculated the parameters for each of the three sets (Figure 2 Step 3); the linearized algorithm is described in Figure S.3 in detail. The final EEC parameters were calculated for Figure 2 Step 4 by averaging the results from Step 3.

The averaging of the EEC parameters assumed two requirements. First, that all measured impedance values were in a frequency range corresponding to the kinetic arc of the spectra. Second, that there was no distribution of time constants within the kinetic arc of the spectra (e.g., constant phase element) and, therefore, that the EEC contained a pure capacitance. Additionally, the accuracy of the IRTM methodology increases when the measurement frequencies have a reduced spacing. The larger the difference between the (at least 3) measurement frequencies, the larger the error of the IRTM methodology (see Figure S.6). Due to the analytic nature of the data processing algorithm, the calculation time was negligible compared to the time necessary to record the impedance data. The time interval for the real-time monitoring was limited by the impedance data measured at the lowest frequency (120 Hz in this work).

## Experimental Details

### Cell Set-up

A lab size and an automotive size PEMFC were used to validate the aforementioned IRTM approach. The cell set up is illustrated in

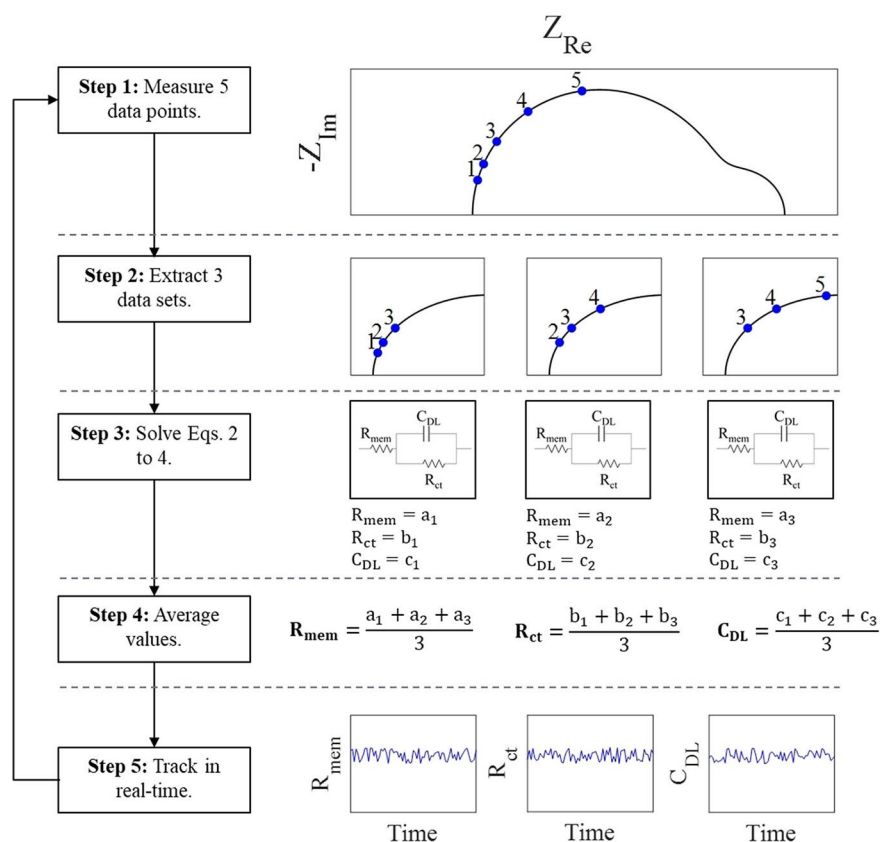


**Figure 2.** The flow chart illustrating the Impedance Real-Time Monitoring (IRTM) methodology. In Step 1, five impedance values at different frequencies were measured. Afterwards, three corresponding data sets were extracted from these measurements, as shown in Step 2. The analytical IRTM calculation (see Figure S.3) extracted values for the membrane resistance ( $R_{\text{mem}}$ ), charge transfer resistance ( $R_{\text{ct}}$ ) and the double layer capacitance ( $C_{\text{DL}}$ ). These values were averaged in Step 4 and could be tracked and further analyzed in real time (Step 5).

Figure S.1. The active areas were  $43.56\text{ cm}^2$  and  $285\text{ cm}^2$  for the automotive and lab size cell, respectively. Both MEAs were provided by Johnson Matthey Fuel Cells. Commercial gas diffusion layers (GDL) of SGL Carbon SE were used for both cells. 29 BC (thickness  $235\text{ }\mu\text{m}$ ) was used at both electrodes of the lab size cell. The same GDL was used for the anode of the automotive size cell. At the cathode, a special designed GDL (22 BB) with a thickness of  $220\text{ }\mu\text{m}$  was used. The membrane of both MEAs had a thickness of  $15\text{ }\mu\text{m}$ . Filtered air and hydrogen with a purity of 99.999% were used to operate the fuel cell.

### Test Procedure

To validate the IRTM methodology, experiments were carried out using the lab and automotive size PEMFCs. Automotive operational parameter ranges were extracted from system models and implemented at the test rig.<sup>[40]</sup> A variation of the operational parameters (cell temperature  $T$ , cell current density  $i$ , cell humidification  $RH$ , air/hydrogen pressure  $p$  and air/hydrogen "stoichiometry",  $\lambda$ ) was conducted using a lab and an automotive size single cell.

For parameter variations using the automotive cell, at each set of humidification and cell temperature (e.g.,  $RH=0.55$  and  $T=65^\circ\text{C}$ ) four different current densities ( $0.5, 1.0, 1.5$  and  $2.0\text{ A cm}^{-2}$ ) were approached. At each current density the gas pressures of anode and cathode, as well as the hydrogen and air stoichiometry were varied successively. During variation of pressure or stoichiometry all other (controllable) operational parameters were kept constant at a certain value, as indicated in Table 1. The corresponding test protocol for the automotive size cell is illustrated in Figure 3. The test protocol of the lab size cell was similar (see supporting information Figure S.2). During the parameter variations, EIS at 326 different operational parameter sets were recorded using the lab size cell and 598 – using the automotive size one. At each operational parameter set, an impedance spectrum between 0.3 and 1000 Hz was measured. One typical EIS is shown by way of example in Figure 4A.

FC malfunctions can occur during system operation and are the main reason for limited system lifetime and performance. Fuel starvation is one of the most critical faulty operational modes since it promotes degradation of the support and catalyst layers.<sup>[41,42]</sup> Oxygen starvation increases heterogeneities in local potentials and decreases the fuel cell's lifetime and performance.<sup>[43]</sup> Dehydration and flooding of the membrane and catalyst layers accelerates membrane degradation due to mechanical stress and induces other degradation mechanisms such as media starvations.<sup>[43]</sup> Therefore, the IRTM responses obtained under the fuel starvation, oxygen starvation, and dehydration conditions were tested within this study. Dehydration of the polymer was tested by operating the cell at low gas humidification and high air volume flows (see Table 2, increasing air supply). Additionally, the impact of oxygen starvation within the catalyst layer was tested by decreasing the "oxygen

**Table 1.** This table lists the parameter range of stoichiometries and gas outlet pressures during the parameter variation experiment. The column "Constant Value" lists operational parameters that were held constant while another operational parameter was varied. The column "Variation Range" lists the variation range of the corresponding operational parameter.

Operational parameter	Unit	Constant Value	Variation Range
Hydrogen Stoichiometry	–	1.75	1.2–1.75
Air Stoichiometry	–	2.2	1.4–2.4
Hydrogen pressure @ outlet	bar <sub>abs</sub>	2.0	1.8–2.1
Air pressure @ outlet	bar <sub>abs</sub>	1.8	1.7–2.0

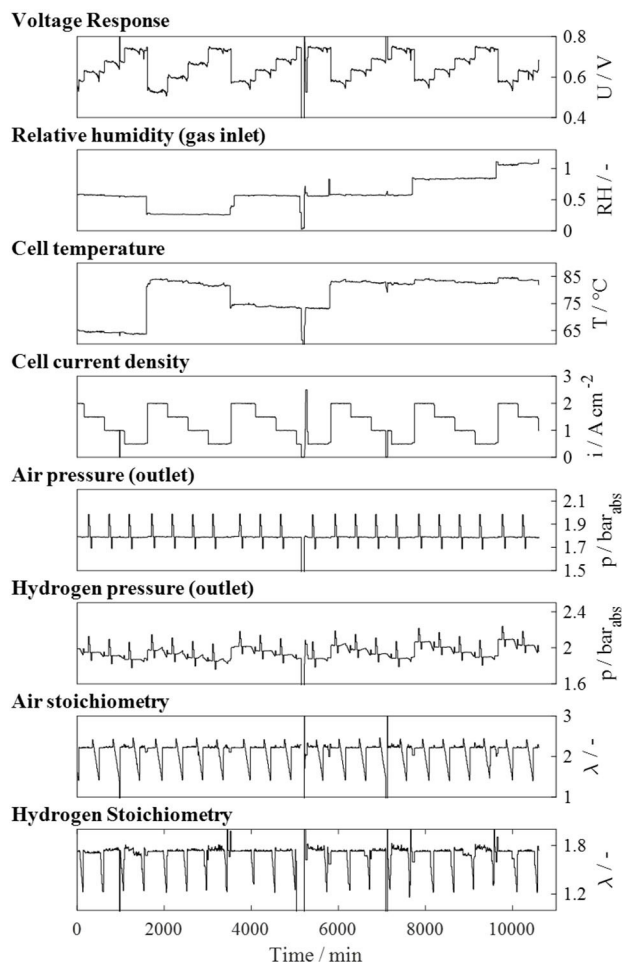


**Figure 3.** This figure illustrates the operational conditions during the parameter variation of the automotive size PEMFC. The top graph shows the corresponding cell voltage. In total 598 impedance spectra between 0.3 and 1 kHz were recorded during this procedure at each operational parameter set. The values corresponding to the parameter variations of stoichiometry  $\lambda$  and pressure  $p$  are in detail listed in Table 1.

**Table 2.** This table lists the operational conditions used to trigger failure modes for the automotive PEMFC experiment. The air supply was limited and increased in order to induce various failure mechanisms like air starvation and polymer dehydration, respectively. The hydrogen supply was limited to trigger local and global hydrogen starvation. During the air supply variation (between  $\lambda_{\text{Air}}=1.6$  and  $\lambda_{\text{Air}}=1.1$ ) the hydrogen stoichiometry was constant at 1.9 (in bold print). During the hydrogen supply variation (between  $\lambda_{\text{H}_2}=1.9$  and  $\lambda_{\text{H}_2}=1.05$ ), the air stoichiometry was constant at 1.6 (in bold print).

	Limiting air/ H <sub>2</sub> supply	Increasing air supply
Current density/[A cm <sup>-2</sup> ]	0.55	0.7
Inlet gas humidification	0.68	0.11
Anode and cathode/-		
Cell temperature/[°C]	65	85
Hydrogen stoichiometry/-	<b>1.9</b> to 1.05	1.5
Air stoichiometry/-	1.6 to <b>1.1</b>	1.1 to 3.2
Cathode outlet pressure/bar (absolute)	2	1.85
Anode outlet pressure/bar (absolute)	2	2.3
Pressure drop cathode/bar (absolute)	1.3 to 0.09	0.12 to 0.3

### Validation of the Impedance Real-Time Monitoring (IRTM) approach.

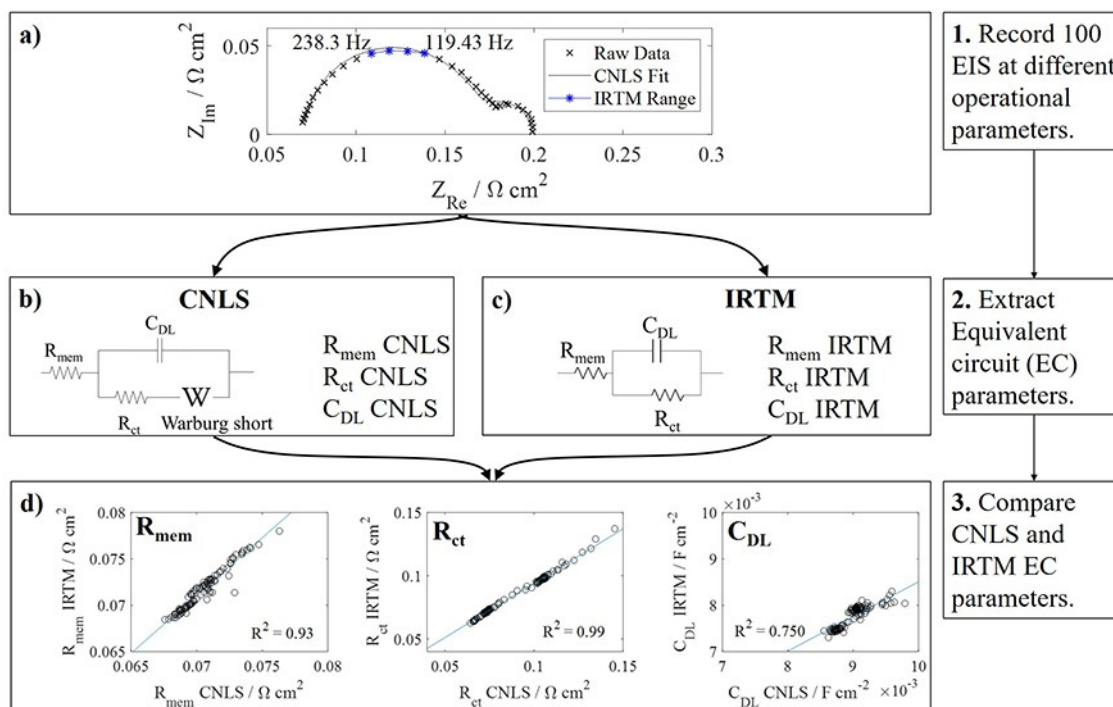


**Figure 4.** This figure illustrates the validation procedure of the Impedance Real-Time Monitoring (IRTM) approach. A) To validate the model, 100 EIS were recorded within a large operational range (see Figure S.2). The figure shows one of those Nyquist plots exemplarily. The blue line indicates 4 impedance values used for the IRTM methodology (see Figure 2). The CNLS fitting (solid line) was performed using the EIS Data Analysis 1.3 software.<sup>[45]</sup> B) The equivalent electric circuit used to fit the EIS data. C) The local operating model for the analytical IRTM calculations. D) A comparison of the equivalent circuit parameters  $R_{\text{mem}}$  (left),  $R_{\text{ct}}$  (middle) and  $C_{\text{DL}}$  (right) obtained from the CNLS fitting (x-axis) and IRTM calculation (y-axis) for 100 EIS. A linear fit of each set of the data was performed, and the corresponding  $R^2$  values are shown in the graph quantifying the IRTM analysis quality.

stoichiometry" (see Table 2, limiting air supply); a similar procedure was carried out to analyze the impact of hydrogen starvation on the IRTM response (see Table 2, limiting  $\text{H}_2$  supply).

## 2. Results and Discussion

### 2.1. Validation of the Impedance Real-Time Monitoring Approach

The "bounded" Randles model (see Figure 4B)<sup>[44]</sup> was used to fit 100 of the measured EIS sets using a CNLS fitting algorithm.<sup>[45]</sup> The EIS were recorded during the parameter variation (similar to Figure 3) at different current densities (1.0 to 2.0  $\text{A cm}^{-2}$ ), cell humidification (0.26 to 1.09) as well as media pressures and stoichiometries according to Table 1. The membrane resistance,  $R_{\text{mem}}$ , the charge transfer resistance,  $R_{\text{ct}}$ , and the double layer capacitance,  $C_{\text{DL}}$ , were thus extracted. The same EIS EEC parameters were calculated using the IRTM methodology (see Figure 4C) and using only 4 frequencies between 120 and 238 Hz. The higher the measurement frequency, the higher the interference due to the inductances of the FC system was. Therefore, 238 Hz was chosen as the highest frequency limit. Figure 4D compares 100 EIS processed using traditional CNLS fitting and the IRTM methodology. The  $R_{\text{mem}}$  and  $R_{\text{ct}}$  values

extracted from IRTM calculation and CNLS fitting showed similar results. Therefore, these resistances can be measured with high accuracy using the IRTM methodology. The double layer capacitance obtained by IRTM had a somewhat weaker correlation with the CNLS fitting values. Although in this work CNLS fit used a capacitance that was independent of the perturbation frequency, the real capacitance of a PEMFC is dependent on frequency within a wide frequency range. Therefore, the constant phase elements were typically used instead of a double layer capacitance. This can explain lower correlation shown in Figure 2D for the double layer capacitance.

Based on the IRTM methodology, the EEC parameters during the parameter variation of the automotive size cell (see Figure 3) were extracted. The dependence of the membrane resistance, charge transfer resistance and double layer capacitance on current density  $i$  and cell temperature  $T$  is illustrated in Figure 5. The membrane resistance was barely affected by current density at a constant humidification (Figure 5A), as reported in literature.<sup>[36]</sup> The charge transfer resistance decreases with increasing temperature. This trend was also observed in the literature.<sup>[23,46]</sup> The double layer capacitance was rather constant throughout the whole parameter variation (Figure 5C). The trends of the EEC parameters in Figure 5 were

in agreement with literature findings. The dependence of the EEC parameters on relative humidity can be found in Figure S.4.

In summary, the analytical IRTM methodology showed results similar to those of conventional CNLS fitting algorithms (Figure 4D). Additionally, using the IRTM methodology during operation of an automotive size fuel cell to extract EEC parameters, showed results similar to those reported in the literature (Figure 5).

## 2.2. Failure Detection using the Impedance Real-Time Monitoring Approach

Figure 6A illustrates the behavior of the cell voltage, “air stoichiometry”, and EIS EEC elements when limiting the air supply. Initially, the cell voltage was stable at an air stoichiometry of 1.6. When decreasing the air stoichiometry down to 1.2, the cell voltage dropped from 0.73 V to 0.65 V and became unstable. The operational conditions at the cathode side enhanced flooding of the cathode. This explains the instabilities seen in the cell voltage. The membrane resistance  $R_{\text{mem}}$  remained constant throughout the experiment. However, the charge transfer resistance  $R_{\text{ct}}$  increased with a decreasing air

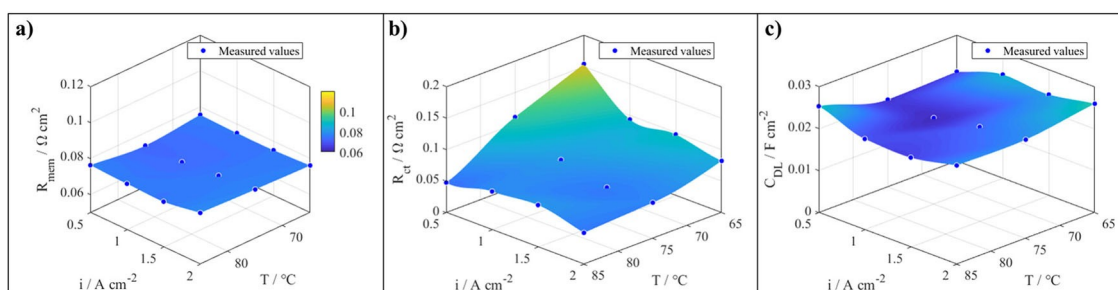


**Figure 5.** This figure illustrates Impedance Real-Time Monitoring results of an automotive size single cell (285 cm<sup>2</sup>) during the parameter variation illustrated in Figure 3. The plots show the dependence of the electrical circuit parameters on current density  $i$  and cell temperature  $T$ . A) Membrane resistance  $R_{\text{mem}}$ . B) Charge transfer resistance  $R_{\text{ct}}$ . C) Double layer capacitance  $C_{\text{DL}}$ . Other operational parameters were constant ( $\lambda_{\text{H}_2} = 1.75$ ,  $\lambda_{\text{Air}} = 2.2$ ,  $\text{RH}_{\text{gas,inlet}} = 0.55$ ,  $p_{\text{H}_2} = 2.0$  bar<sub>abs</sub>,  $p_{\text{Air}} = 1.8$  bar<sub>abs</sub>).

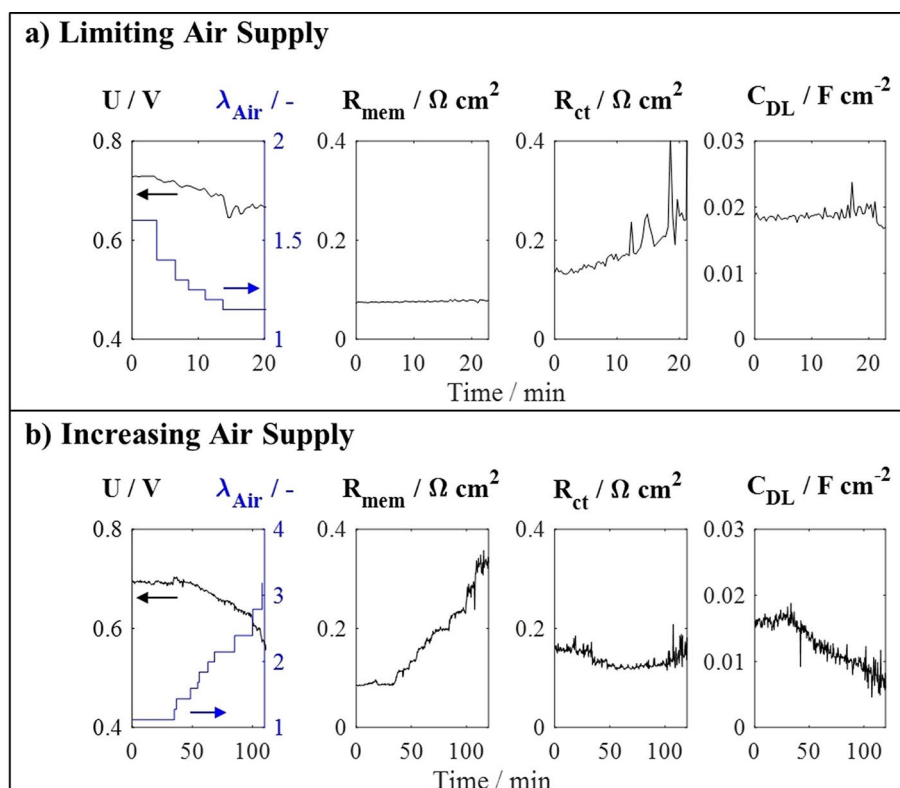


**Figure 6.** Illustration of the impedance real time monitoring of an automotive size single cell according to Table 2 when A) limiting the air supply and B) dehydration of the cell by increasing the air supply (“air stoichiometry”,  $\lambda_{\text{air}}$ ). The corresponding Nyquist plots can be found in Figure S.7.

stoichiometry. An increase in  $R_{ct}$  along with decreasing oxygen partial pressure is often reported in the literature<sup>[7,47,48]</sup> using other impedance-based evaluation and measurement techniques. The change in the  $R_{ct}$  during the air starvation experiment was larger than that of the parameter variation (Figure 5B). The double layer capacitance  $C_{DL}$  remained rather constant throughout the air starvation experiment.

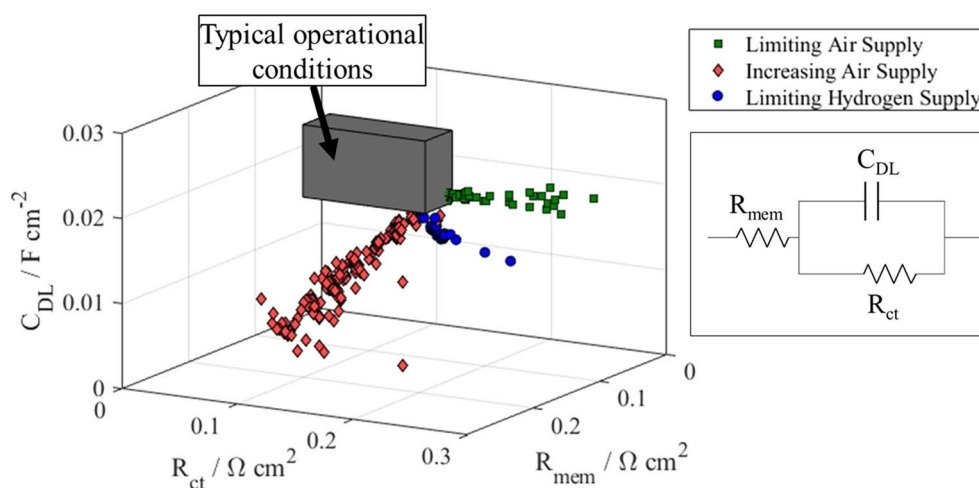
Figure 6B illustrates the results of the measurements for the polymer dehydration resulting from an increase in air supply. With increasing air flow, the cell voltage dropped from 0.69 V to 0.58 V. The membrane resistance  $R_{mem}$  increased with an increase in air stoichiometry and exceeded  $\sim 0.35 \Omega \text{ cm}^2$  during this polymer dehydration experiment (Figure 6B). During normal operation  $R_{mem}$  values were between 0.06 and  $0.11 \Omega \text{ cm}^2$  (see Figure 5A and Figure S.4D). The charge transfer resistance  $R_{ct}$  initially decreased only slightly.  $R_{ct}$  also decreased when increasing the air stoichiometry during the normal operation; this trend is also confirmed by the literature.<sup>[7,47]</sup> The double layer capacitance  $C_{DL}$  significantly dropped from 0.016 to  $0.006 \text{ F cm}^{-2}$  (Figure 6B). This behavior was often difficult to explain since the double layer capacitance is affected by many parameters in such a complex system. Further investigations need to be carried out in order to determine the fundamental origin of this double layer capacitance behavior.

Figure 7 compares the EEC parameters as measured during the FC failures (Figure 6) with the EEC elements measured during the parameter variation (Figure 5) of the automotive size cell. The grey box in Figure 7 marks the range of  $R_{mem}$ ,  $R_{ct}$  and  $C_{DL}$  during typical PEMFC operation. The boundary values of the grey box were defined using the minimum and maximum EEC parameters extracted during the parameter variation (see, e.g., Figure 5 and Figure S.4). Increasing air supply, limiting air supply, and limiting hydrogen supply can be clearly distinguished from typical FC operation since in all three cases at least one of the impedance EEC parameters was significantly higher or lower than during any typical operational parameter

set. In Figure 7 the three different failure modes showed a different behavior of the EEC parameters. It is important to mention that each data point in Figure 7 relied on the impedance at 4 frequencies between 120 and 238 Hz evaluated using the IRTM approach presented here. This allows the impedance based evaluation of transient operation during failure operation. Figure 7 indicates that the IRTM methodology allows a real-time differentiation between polymer dehydration, hydrogen, and air starvation by analyzing  $R_{mem}$ ,  $R_{ct}$  and  $C_{DL}$ . However, the exact physical origin of this differentiation needs to be investigated. The IRTM methodology as illustrated in Figure 2 would allow a clear distinction between different media starvations and dehydration of the cell in real time, as illustrated in Figure 7.

### 3. Conclusions

In conclusion, this work demonstrates that the IRTM methodology is a fast and accurate tool for use in the on-road monitoring of automotive size fuel cells. The IRTM methodology combines the advantages of the fast measurement and stable data processing when using only few frequencies and provides the accuracy close to that typical of the iterative fitting procedures. The IRTM data evaluation is based on a simple Randles circuit with parameters that are frequently used and well understood. This largely simplifies data interpretation. No fitting algorithms are necessary to process the impedance data and, therefore, a "definite answer" is guaranteed as the result of this approach. The lowest measurement frequency used in this work was in the range of 120 Hz and, therefore, the data acquisition and their evaluation should only take from about 50 to 100 ms. The use of a dynamic impedance spectroscopy can further decrease the measurement time. Therefore, the approach presented is able to deal with relatively quick fluctuations in the automotive PEMFC systems and provide real-time



**Figure 7.** Comparison of the span of impedance parameters during normal operation (taken from Figure 5 and Figure S.4) with the span of impedance values during the failure modes. The figure also compares the effect of different failure mechanisms on the membrane resistance  $R_{mem}$ , the charge transfer resistance  $R_{ct}$  and the double layer capacitance  $C_{DL}$ . The right image illustrates the electrical equivalent circuit used in the IRTM model (see Figure 2) used for calculating the impedance parameters.

information about the fuel cell stack. The frequency range between 120 Hz and 238 Hz was identified as a reliable interval which was not affected by the system inductances and low frequency diffusional effects. However, the impact of ageing effects on this frequency range needs to be further evaluated. Furthermore, the influence of severe failure mechanisms like cell voltage reversal or flooding on the analysis needs to be further analyzed.

## Author Contributions

The manuscript was written through contributions of all authors. All authors have given approval to the final version of the manuscript.

## Acknowledgment

The project (INSPIRE) has received funding from the Fuel Cells and Hydrogen 2 Joint Undertaking under grant agreement No 700127. This Joint Undertaking receives support from the European Union's Horizon 2020 research and innovation program, Hydrogen Europe and Hydrogen Europe Research. Financial support from German Research Foundation (DFG) under Germany's Excellence Strategy-EXC 2089/1-390776260, cluster of excellence "e-conversion" is gratefully acknowledged. Open access funding enabled and organized by Projekt DEAL.

## Conflict of Interest

The authors declare no conflict of interest.

**Keywords:** fuel cells · electrochemical impedance spectroscopy · automotive · online diagnostics · energy conversion

- [1] BMW Group, "The BMW i Hydrogen NEXT at the IAA Cars 2019", can be found under <https://www.press.bmwgroup.com/global/article/detail/T0300507EN/the-bmw-i-hydrogen-next-at-the-iaa-cars-2019>, 2019.
- [2] J. Shin, W.-S. Hwang, H. Choi, *Technol. Forecast. Soc. Change* **2019**, *143*, 239–248.
- [3] I. Staffell, D. Scamman, A. V. Abad, P. Balcombe, P. E. Dodds, P. Ekins, N. Shah, K. R. Ward, *Energy Environ. Sci.* **2019**, *12*, 463–491.
- [4] T. Sutharssan, D. Montalvao, Y. K. Chen, W.-C. Wang, C. Pisac, H. Elemara, *Renewable Sustainable Energy Rev.* **2017**, *75*, 440–450.
- [5] R. Borup, J. Meyers, B. Pivovar, Y. S. Kim, R. Mukundan, N. Garland, D. Myers, M. Wilson, F. Garzon, D. Wood, P. Zelenay, K. More, K. Stroh, T. Zawodzinski, J. Boncella, J. E. McGrath, M. Inaba, K. Miyatake, M. Hori, K. Ota, Z. Ogumi, S. Miyata, A. Nishikata, Z. Siroma, Y. Uchimoto, K. Yasuda, K.-C. Kimjima, N. Iwashita, *Chem. Rev.* **2007**, *107*, 3904–3951.
- [6] N. Fouquet, C. Doulet, C. Nouillant, G. Dauphin-Tanguy, B. Ould-Bouamama, *J. Power Sources* **2006**, *159*, 905–913.
- [7] C. Brunetto, A. Moschetto, G. Tina, *Electr. Power Syst. Res.* **2009**, *79*, 17–26.
- [8] H. Nakajima, T. Kitahara, *Heat Mass Transfer* **2018**, *54*, 2551–2558.
- [9] C. Jeppesen, S. S. Araya, S. L. Sahlén, S. Thomas, S. J. Andreasen, S. K. Kær, *J. Power Sources* **2017**, *359*, 37–47.
- [10] N. Fouquet, *2010 IEEE VPPC* **2010**, 1–8.
- [11] T. Kurz, A. Hakenjos, J. Krämer, M. Zedda, C. Agert, *J. Power Sources* **2008**, *180*, 742–747.
- [12] N. Kitamura, K. Manabe, Y. Nonobe, M. Kizaki, *SAE [Tech. Pap.]* **2010**, DOI 10.4271/2010-01-1088.
- [13] M. A. Rubio, A. Urquia, S. Dormido, *Int. J. Hydrogen Energy* **2010**, *35*, 2586–2590.
- [14] P. Kurzweil, H. J. Fischle, *J. Power Sources* **2004**, *127*, 331–340.
- [15] T. Ogawa (Toyota Jidosha Kabushiki Kaisha), Y. Naganuma (Toyota Jidosha Kabushiki Kaisha), US 9 793 561 B2, **2017**.
- [16] T. H. Min (Hyundai Autron Co., Ltd.), US 9 945 911 B2, **2018**.
- [17] M. Matsumoto (Nissan Motor Co., Ltd.), K. Hoshi (Nissan Motor Co., Ltd.), T. Aoki (Nissan Motor Co., Ltd.), US 10 177 391 B2, **2019**.
- [18] M. Sinha (GM, Global Technology Operations LLC), P. A. Rapaport (GM Global Technology Operations LLC), H. Yoshida (Honda Motor Co., Ltd.), S. Toyota (Honda Motor Co., Ltd.), Y.-H. Lai (GM Global Technology Operations LLC), US 10 218 018 B2, **2019**.
- [19] G. Wang, Y. Yu, H. Liu, C. Gong, S. Wen, X. Wang, Z. Tu, *Fuel Process. Technol.* **2018**, *179*, 203–228.
- [20] H. Wang, A. Gaillard, D. Hissel, *Renewable Energy* **2019**, *141*, 124–138.
- [21] J. P. Schmidt, T. Hammerschmidt in *Automobil-Sensorik 2*, Vol. 1 (Eds.: T. Tille), Springer Vieweg, Berlin, Heidelberg, **2018**, pp. 99–126.
- [22] G. Dotelli, R. Ferrero, P. Gallo Stampino, S. Latorrata, S. Toscani, *IEEE Trans. Instrum. Meas.* **2016**, *65*, 1007–1014.
- [23] S. J. Andreasen, J. Rabjerg Vang, S. K. Kær, *Int. J. Hydrogen Energy* **2011**, *36*, 9815–9830.
- [24] Y. Yu, H. Li, H. Wang, X.-Z. Yuan, G. Wang, M. Pan, *J. Power Sources* **2012**, *205*, 10–23.
- [25] A. Taniguchi, T. Akita, K. Yasuda, Y. Miyazaki, *J. Power Sources* **2004**, *130*, 42–49.
- [26] A. S. Bondarenko, *Anal. Chim. Acta* **2012**, *743*, 41–50.
- [27] B. Sanchez, A. S. Bandarenka, G. Vandersteen, J. Schoukens, R. Bragos, *Med. Eng. Phys.* **2013**, *35*, 1349–1357.
- [28] S. Thomas, S. C. Lee, A. K. Sahu, S. Park, *Int. J. Hydrogen Energy* **2014**, *39*, 4558–4565.
- [29] N. J. Steffy, S. Vinod Selvaganesh, M. Kumar, A. K. Sahu, *J. Power Sources* **2018**, *404*, 81–88.
- [30] T. Kadyk, R. Hanke-Rauschenbach, K. Sundmacher, *Int. J. Hydrogen Energy* **2012**, *37*, 7689–7701.
- [31] E. Ivers-Tiffée, A. Weber, *J. Ceram. Soc. Jpn.* **2017**, *125*, 193–201.
- [32] C. Jeppesen, S. S. Araya, S. L. Sahlén, S. J. Andreasen, S. K. Kær, *Int. J. Hydrogen Energy* **2017**, *42*, 15851–15860.
- [33] D. Aaron, S. Yiacoymi, C. Tsouris, *Sep. Sci. Technol.* **2008**, *43*, 2307–2320.
- [34] S. M. R. Niya, M. Hoorfar, *J. Power Sources* **2013**, *240*, 281–293.
- [35] D. Malevich, E. Halliop, B. A. Peppley, J. G. Pharoah, K. Karan, *J. Electrochem. Soc.* **2009**, *156*, B216–B224.
- [36] M. A. Danzer, E. P. Hofer, *J. Power Sources* **2009**, *190*, 25–33.
- [37] D. Vladikova, Z. Stoyanov, *J. Electroanal. Chem.* **2004**, *572*, 377–387.
- [38] I. A. Schneider, S. A. Freunberger, D. Kramer, A. Wokaun, G. G. Scherer, *J. Electrochem. Soc.* **2007**, *154*, B383–B388.
- [39] X. Yuan, H. Wang, J. C. Sun, J. Zhang, *Int. J. Hydrogen Energy* **2007**, *32*, 4365–4380.
- [40] T. Lochner, L. Hallitzky, M. Perchthaler, M. Obermaier, J. Sabawa, S. Enz, A. S. Bandarenka, *Appl. Energy* **2020**, *260*, 114291.
- [41] C. A. Reiser, L. Bregoli, T. W. Patterson, J. S. Yi, J. D. Yang, M. L. Perry, T. D. Jarvi, *Electrochem. Solid-State Lett.* **2005**, *8*, A273–A276.
- [42] N. Yousfi-Steiner, P. Moçotéguy, D. Candusso, D. Hissel, *J. Power Sources* **2009**, *194*, 130–145.
- [43] P. Pei, H. Chen, *Appl. Energy* **2014**, *125*, 60–75.
- [44] J. P. Sabawa, A. S. Bandarenka, *Electrochim. Acta* **2019**, *311*, 21–29.
- [45] A. S. Bandarenka in *Lecture Notes on Impedance Spectroscopy. Measurement, Modeling and Applications*, Vol. 4 (Eds.: O. Kanoun), CRC Press, Taylor and Francis Group, London, **2013**, pp. 29–36.
- [46] S. Asghari, A. Mokmeli, M. Samavati, *Int. J. Hydrogen Energy* **2010**, *35*, 9283–9290.
- [47] J. Zhang, Y. Tang, C. Song, J. Zhang, *J. Power Sources* **2007**, *172*, 163–171.
- [48] S. M. R. Niya, R. K. Phillips, M. Hoorfar, *J. Electroanal. Chem.* **2016**, *775*, 273–279.

Manuscript received: April 6, 2020

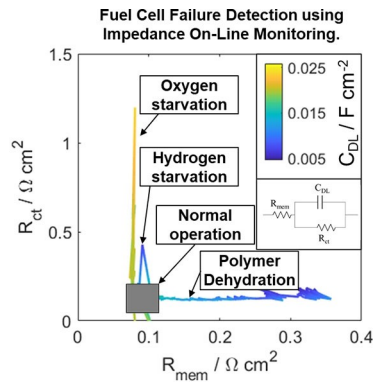
Revised manuscript received: June 8, 2020

Accepted manuscript online: June 9, 2020



# ARTICLES

**Finding faults:** Real-time monitoring of automotive-size fuel cells based on electrochemical impedance spectroscopy using a differential impedance analysis data post-processing approach shows high selectivity to detect prominent fuel cell malfunctions.



*T. Lochner\**, *Dr. M. Perchthaler*, *J. T. Binder*, *J. P. Sabawa*, *T. A. Dao*,  
*Prof. A. S. Bandarenka\**

1 – 9

**Real-Time Impedance Analysis for the On-Road Monitoring of Automotive Fuel Cells**

